

Supporting Information:

Antiferromagnet–semiconductor van der Waals heterostructures: interlayer interplay of exciton with magnetic ordering

Masaru Onga^{1,2}, Yusuke Sugita², Toshiya Ideue^{1,2}, Yuji Nakagawa^{1,2}, Ryuji Suzuki^{1,2}, Yukitoshi Motome², Yoshihiro Iwasa^{1,2,3,*}

¹ Quantum-Phase Electronics Center (QPEC), The University of Tokyo, Tokyo 113-8656, Japan

² Department of Applied Physics, The University of Tokyo, Tokyo 113-8656, Japan

³ RIKEN Center for Emergent Matter Science (CEMS), Wako 351-0198, Japan

*Correspondence to: iwasa@ap.t.u-tokyo.ac.jp

§1. Magnetic structures of MPX_3

MPX_3 family (M : transition metals, X : chalcogenides) shows various types of magnetic ordering¹. The spin orderings occur at honeycomb M^{2+} within the layer: for instance, $MnPS_3$ has the Néel-type spin ordering parallel to c-axis at Mn^{2+} ions, while $FePS_3$ and $FePSe_3$ have the zigzag-type orderings also along c-axis at Fe^{2+} ions.

The magnetic moment of the Néel-type $MnPSe_3$ is supposed to lie within the basal plain (or slightly canted between the plain and c-axis) according to the neutron diffraction study on polycrystalline powder². In our calculation shown later in §9, however, the monolayer $MnPSe_3$ beneath the monolayer TMDs has an easy axis along c-axis similarly to the previous first-principal calculation on a bilayer $MnPSe_3$ ³. We have no conclusive picture of the actual spin ordering at the surface of $MnPSe_3$ due to the above controversy and the experimental difficulty to detect it.

We can guess that the heterostructure made of $MnPS_3$ (with Neel-type Mn^{2+}) would show the similar effects to that of $MnPSe_3$. However, the situation could be dramatically distinct because of the different orientations of sublattice spins in bulk

MnPS₃ (along c-axis) and bulk MnPSe₃ (almost lied in ab-plane) as we noted above. Since the magnetoresponse of the TMDs is quite anisotropic owing to the Zeeman-type spin-splitting at the K-points, the excitons at the interface with antiferromagnets can also be sensitive to the spin-orientation of the magnets as well as the types of spin-ordering. It would be very informative to explore the detailed experiments with other MPX₃ in order to elucidate the microscopic coupling at the interface. The direction of the sublattice magnetic moments can also explain the M -dependency of the exciton-magnon interaction discussed in Fig.4 of the main text.

§2. Commensurability depending on stacking angles

The 2×2 superlattice of MoSe₂ (lattice constant $a_{\text{MoSe}_2} = 0.328$ nm) and the unit-cell of MPSe₃ (exactly speaking $M_2P_2Se_6$, $a_{\text{Mn}_2P_2Se_6} = 0.639$ nm and $a_{\text{Fe}_2P_2Se_6} = 0.632$ nm) present nearly commensurate lattice matching with the parallel configuration: their lattice mismatches are 2.6% in MnPSe₃ and 3.6% in FePSe₃ as calculated from the lattice constants of bulk. Figure S1a shows the image of MoSe₂/MnPSe₃ in the parallel case. In contrast, we cannot expect the good lattice matching with the perpendicular configuration as shown in Fig. S2b, visually presenting moiré patterns in this case within this scale. In the parallel case, we cannot see moiré patterns in the scale of Fig. S1a (~ 20 unit cells of MoSe₂) due to the relatively small lattice mismatch of 2.6%, meaning that more than 80 unit cells are needed to see such a periodic pattern.

§3. Detailed discussions on Raman spectra

We show Raman spectra around 222cm^{-1} at various temperatures in Fig. S2 as raw data of Fig. 2c in the main text. The abrupt changes around $T_N=74$ K of the bulk

MnPSe₃ support that the antiferromagnetic transition of the exfoliated MnPSe₃ occurs at almost same temperature as the bulk^{2,4}. Similar behavior is also observed in the peaks around 149 and 175 cm⁻¹.

Generally speaking, two-magnon scattering can cause a broad Raman peak at the two-magnon frequency at Brillouin zone boundary ($\sim 9 \text{ meV} \times 2 = 145 \text{ cm}^{-1}$ in MnPSe₃³). A recent study on Raman spectroscopy of bulk/exfoliated MnPS₃ reports a small two-magnon peak above 2.71 eV-excitation in a bulk sample⁵. However, no two-magnon peak has been observed within our measurements with 2.33 eV-excitation. Considering the previous work mentioned above⁵, it could be due to the small excitation energy and/or weaker intensity of the two-magnon peak in exfoliated flakes than a prominent phonon peak around 149 cm⁻¹.

§4. PL spectra from MoSe₂/MPSe₃: Possible moiré excitons and strain from substrates

Figure S3 display four PL spectra of sample F1 (MoSe₂/FePSe₃, ||), A1 (MoSe₂/FePSe₃, ||), S1 (MoSe₂/SiO₂), E1 (MoSe₂/MnPSe₃, ⊥), and G1 (MoSe₂/FePSe₃, ⊥) at 6 K. We also plot the fitting results by multi-peaks Voigt function: the spectra of sample F1, A1 and S1 can be decomposed well into two peaks, while that of sample E1 and G1 includes more peaks. Here we discuss the origins and positions of the peaks in detail.

Following the previous study on MoSe₂/SiO₂⁶, the peaks at the highest energy in each spectrum are attributed to the neutral excitons (X^0), while the peaks located 30 meV lower than X^0 are assigned as the charged excitons (trions, X^T). Only in the spectrum of the perpendicular configuration of MoSe₂/(Mn, Fe)PSe₃ (sample E1, E2 and G1), we found an unknown peak (X^M) located at 10 ~ 15 meV lower than X^0 . This middle peak X^M is assigned as neither trions nor neutral biexcitons, because the binding

energies from the X^0 state are 30 meV both for positively and negatively charged trions regardless of the doping level⁶ and 20 meV for neutral biexcitons⁷. This suggests that the X^M is likely attributed to moiré excitons affected by the moiré potential at the interface (shown in Fig. S2b) as discovered in TMD-TMD heterostructures⁸⁻¹¹.

Regarding sample G1 (MoSe₂/FePSe₃, perpendicular) in Fig. S3, the spectrum appears complicated and includes multiple peaks, some of which are absent in sample F1 (MoSe₂/FePSe₃, parallel). For peak extraction, we assumed here that the spectrum of G1 should be composed of X^0 and X^T which exist all other spectra (with the constant trion binding energy (35 meV)), and then found to be decomposed into four peaks (X^0 , X^T , and other two peaks) by fitting. One of them is located at X^M of sample E1, so we also named it X^M of G1 after that of E1. The last and lowest peak is unknown, but we assigned it as localized exciton (X^L). X^L has been frequently discussed in MoS₂ (or WSe₂) as a defect-mediated bound state.

The position of each peak can be explained by the lattice mismatch and the consequent innate strain except the antiferromagnetic effect which is mainly discussed in the main text. If the lattice relaxation occurs at the present vdW interface, MPSe₃ induces the compressive strain to the monolayer MoSe₂ in the parallel configuration, while the lattice mismatch on the SiO₂ substrate can be regarded as zero because the surface structure of SiO₂ is amorphous. Lattice reconstruction at the van der Waals interfaces has been directly reported in graphene/BN¹² and graphene/graphene¹³ systems although such reconstruction at vdW interfaces had been assumed to be absent at the early stage of this field. Our fabrication procedure includes annealing at 250 °C (same condition as the report showing the reconstruction at the heterointerface¹²), thus we can expect such lattice relaxation producing strain from the substrates.

Since the compressive strain enlarges the bandgap of TMDs^{14,15}, this mechanism can explain the substrate dependence of the X^0 and X^T positions in Fig. S3; the peak positions line up in order of the lattice mismatch, sample $S1 < A1 < E1$. According to previous studies^{14,15}, the compressive strain is deduced from the observed peaks as 0.5 ~ 1%. The value is less than the lattice mismatch probably because the lattice of the surface of the counterpart $MPSe_3$ can be expanded. Sample E1 shows the peaks of X^0 and X^T at similar positions as sample S1 and thus implies negligibly small strain in $MoSe_2$, being consistent with the nearly incommensurable picture in the perpendicular configuration as shown in Fig. S1b. Note here that we assume the effect of dielectric environment can be negligible because the peak position of $MoSe_2/MnPSe_3 (\perp)$ is not shifted as seen in Fig. S3 even though the dielectric constant of bottom $MnPSe_3$ is identical to $MoSe_2/MnPSe_3 (//)$.

§5. Temperature dependence of the X^0 peaks in $MoSe_2$ on SiO_2

The bandgaps of $MoSe_2$ and other TMDs are known to follow the temperature dependence of standard semiconductors as following¹⁶:

$$E(T) = E_0 - S\hbar\omega \left[\coth\left(\frac{\hbar\omega}{2k_B T} - 1\right) \right] \quad (1)$$

where E_0 is the bandgap (exciton energy) at zero temperature, S is dimensionless coupling constant, and $\hbar\omega$ is an average phonon energy. Figure S4 shows the temperature dependence of sample S1 ($MoSe_2$ on SiO_2) and the fitting curve by (1). We deduced $E_0 = 1.6514$ eV, $S = 1.86$, and $\hbar\omega = 14$ meV, which are similar to the previous report (1.657 eV, 1.96, 15 meV, respectively)⁶. In the main text, we discuss the anomalous peak shifts in addition to this basic temperature dependence.

§6. Temperature dependence in other MoSe₂/MPSe₃ samples

To check reproducibility of the additional shifts below T_N , we fabricated and measured several samples in addition to sample A1, E1, F1, G1 and S1 in the main text. Figure S5 indicating the data from sample A2, A3, E2, S2 totally agrees to the data in Fig. 4, supporting our results are truly intrinsic in the system.

§7. Experimental data of WSe₂/MPSe₃ and MoS₂/MPSe₃ heterointerfaces

We also conducted the experiments using TMDs other than MoSe₂ in order to check the universality of our results among group-VI TMDs. The data shown in Fig. S6 indicate that the phenomena observed in MoSe₂/MPSe₃ occur also in WSe₂/MPSe₃ and MoS₂/MnPS₃ and their features are similar quantitatively and qualitatively among TMDs. It is not easy to discuss their differences among TMDs in detail due to the differences in their lattice constant/band structure/spin-orbit interaction at present.

We note that the extracted peaks from WSe₂ and MoS₂ can include the luminescence from charged excitons and/or localized excitons due to their broadness and complexity of PL peaks while PL peaks from MoSe₂ are sharp enough to separate them clearly into neutral and charged excitons. Especially, further researches on the exciton-magnon interaction in charged excitons could give us a tool to tune the interaction electrically.

§8. Electronic band structure of the heterostructure by DFT calculations

We performed band structure calculations based on the density functional theory (DFT) for the bilayer system composed of monolayer TMD/monolayer MnPS₃. The unit cell used in the calculations is shown in Figs. S7a and b, where we assumed the two Mn atoms are located beneath the Mo and Se atoms, respectively, to model the

nearly commensurate stacking in the case of the parallel configuration discussed in the main text. We adopted MoS₂ as a monolayer TMD because it has a small lattice mismatch ($\sim 1.0\%$) with MnPSe₃¹⁷; we fixed the in-plane lattice constant of the unit cell to 6.390 Å and optimized the atomic positions in the unit cell. In the calculations, we employed the GGA+ U method taking $U = 5$ eV for the d orbitals of Mn, assuming the Néel-type antiferromagnetic order with the magnetic moments along the out-of-plane directions in the honeycomb lattice formed by Mn sites.

The Brillouin zone (BZ) for this system is shown in Fig. S7c. The BZ of the superlattice (black rectangle in Fig. S7c) is one fourth of the original one of MoS₂ (orange rectangle), and hence, the high-symmetric points are defined in the folded positions (e.g., the K and M points indicated by the green letters). Note that the new K point originates from the “ $-K$ point” of the original BZ of MoS₂, and the new Γ -K-M line does not correspond to “the original Γ -K-M line” [e.g., the new Γ -K line does not include the “Q (or Λ) points” of the original MoS₂].

Figure S7d displays the band structure of the MoS₂/MnPSe₃ bilayer. For each electronic band, we indicate the contributions from the d orbitals of Mo and Mn separately by the colored circles. Hereafter, all the origins of the energy are set at the top of the valence bands of MoS₂. The bottoms/tops of the conduction/valence bands from MoS₂ are isolated from the ones of MnPSe₃. We note that our results agree well with the previous results on the same system¹⁷.

§9. Electronic band structure for different magnetic structures

We conducted three kinds of calculations to clarify how the bandgap of MoS₂ is modified by changing the magnetism on the neighboring MnPSe₃ layer. Specifically,

we controlled the direction and amplitude of the magnetic moments, and type of the magnetic ordering of Mn^{2+} .

First, Fig. S8 shows the band structures for different directions of the magnetic moments of the Néel order, \mathbf{m} : parallel to the c axis ($\mathbf{m} // c$) and vertical to the c axis ($\mathbf{m} \perp c$) in Figs. S8a and b, respectively. From the comparison of the total energies, the case with $\mathbf{m} // c$ is slightly more stable than that with $\mathbf{m} \perp c$, as in the ground state of a bilayer MnPSe_3 ². We find that the difference of the bandgaps of MoS_2 between the two cases is very small, less than 0.5 meV, as shown in Fig. S8c. This is one order of magnitude smaller than the PL spectral shift in the main text. We note that in both cases, the conduction band edges of MoS_2 exhibit the Zeeman-type spin polarization (almost aligned along the c -axis).

Next, in Fig. S9, we show the band structures with different amplitudes of the magnetic moments, $m=|\mathbf{m}|$, for the case with $\mathbf{m} // c$. The results were obtained by the GGA+ U calculations with the constraints on the magnetic moments¹⁸. The bandgaps of MoS_2 are hardly modified by the change in the magnetic moments from $4.60 \mu_B$ to $5.73 \mu_B$, as shown in Fig. S9b.

Finally, we compare the band structures for the Néel and zigzag-type antiferromagnetic order in Fig. S10. The calculations are done by assuming the double supercell to incorporate the zigzag-type order (Figs. S10a and b). Note that a similar zigzag order is realized in FePSe_3 . Here, we adopted not GGA+ U but GGA calculations because of the high computational cost for 40 atoms in the supercell. As shown in Fig. S10e, we find no significant difference in the bandgaps of MoS_2 for the different types of antiferromagnetic orders. Note that the additional bands, whose band bottom is lower than 1.570 eV, predominantly originate from Mn d orbitals.

From these results, we conclude that the antiferromagnetic order in MnPSe₃ does not affect the bandgap of MoS₂ significantly. The change of the bandgap for different antiferromagnetic structures is too small to explain the upshift of the PL spectra in the main text. This is in stark contrast to the substantial change in the bandgap for the ferromagnetic substrate suggested theoretically¹⁹. The band alignment would be changed before and after the AFM transition as we can see the change in MnPSe₃ bands in changing the magnetic states (Fig. S8-10). The band alignment, however, does not affect excitonic peak positions inside monolayer TMDs (which is not *interlayer* but *intralayer* exciton) as far as the bandgaps of TMDs themselves are not altered as mentioned above.

§10. Strain effect due to magnetostriction in MnPSe₃

Magnetostriction of the antiferromagnets below T_N can compress the lattice of TMDs, which may potentially explain the observed upshift through a strain effect. The observed shift (~ 5 meV) requires roughly 0.1% compressive strain^{14,15}. However, a previous study on bulk MnPSe₃ showed that the magnetic strain is, if any, one order of magnitude smaller ($< 0.02\%$, below their measurement limit) across T_N except the usual thermal expansion¹. This suggests that the strain induced by magnetostriction on MnPSe₃ cannot explain our experimental results.

To confirm this, we performed the DFT calculations while changing the in-plane lattice constant (Fig. S11). As shown in Fig. S11a, the bandgap of MoS₂ is changed linearly to the lattice constant. Figure S11b shows the total energy comparison of the systems with different lattice constants for different U in the GGA+ U calculations. The result indicates that the larger electron interaction leads to the larger lattice constant in the stable crystalline structure. Since U stabilizes the Néel order, our

results show that the additional strain from the Néel ordering is expected to be tensile, inducing the downshift opposite to the experimental data. Thus, the magnetic strain cannot rationalize our experimental results.

§11. Magnetic polaron effect at the magnetic van der Waals heterointerface

The exciton binding energy in monolayer TMDs could be modified due to the magnetic ordering in MnPSe₃. Magnetic-polaron picture is frequently used to describe the excitonic features in magnetic semiconductors²⁰. This picture, however, also results in the opposite peak shift since the binding energy of excitons gets larger due to the magnetic polaron effect.

Meanwhile, two elementary excitations composing polaronic states can generally interact each other not only attractively (similarly to the bound magnetic polaron in magnetic semiconductors) but also repulsively²¹. If there is strong repulsion between excitonic (high energy) and magnonic (low energy) states in our system, it can explain the upshifts of the excitonic states. Because this mechanism can include exciton-magnon coupling in a broad sense, we don't mention it explicitly in the main text.

The effects on the mass of exciton in TMDs from antiferromagnetic MnPSe₃ is also not likely because the band edge of TMD, which determines the mass of exciton, is not so modulated directly by MnPSe₃ as discussed in §7 and §8.

§12. Interlayer exciton-magnon coupling at the heterointerfaces

In the main text, we attribute the observed shift to the effect of the interlayer exciton-magnon interaction. According to previous studies in a single material, the

form of Hamiltonian inducing the exciton-magnon interaction (\mathcal{H}_{EMC}) under radiative electric field (\vec{E}) can be written as

$$\mathcal{H}_{\text{EMC}} = (\vec{\pi} \cdot \vec{E}) a^\dagger c^\dagger + h.c. \quad (2)$$

where $\vec{\pi}$ is coupling constant related to the exchange interaction between the ions, a^\dagger is the exciton creation operator, and c^\dagger is the magnon creation operator^{22,23}. This original theory on exciton-magnon state in d-d transition is based on the electric dipole moment generated by the combination of orbital excitation (exciton) at one sublattice and spin excitation (magnon) at the other sublattice. The dipole moment makes the strong optical transition allowed and strong sideband peaks appear below the T_N ^{22,23}. This theory is similar to the theory on two-magnon process (spin excitations at both sublattices) and exciton-phonon coupling.

In the interlayer EMC, naïvely thinking, we can regard a^\dagger as the exciton creation operator at the TMD layer, c^\dagger as the magnon creation operator at the MnPSe₃ layer, and $\vec{\pi}$ as interlayer coupling constant linked to the exchange coupling between TMDs and MnPSe₃. Note that the exchange couplings between TMDs and ferromagnetic surfaces were confirmed in the recent studies as mentioned in the main text^{24,25}.

However, it is challenging to construct an appropriate theory in more detailed. First, although the exciton-magnon states in d-d transitions (electrical-dipole forbidden/magnetic-dipole allowed) are quite well understood, those in charge transfer transition (electrical-dipole allowed, same as exciton in TMDs) are much less investigated even in bulk as far as we know. It would be quite important to establish the detailed theory about exciton-magnon states in electrical-dipole allowed transitions with originally large oscillator strength.

The original formula (2) is originally made for an exciton and a magnon at localized d-orbitals in one substance. In the heterointerface, however, the magnon and

exciton exist in separated layers and are supposed to interact via interlayer exchange coupling. Moreover, the exciton in TMDs is Wannier excitons which is not localized at the atomic sites and distinct from Frenkel excitons in localized d-electron system. These situations can make it complicated and/or interesting to construct the microscopic theory of the interlayer exciton-magnon coupling.

As a result of (2), energy conservation leads to the simple relation in the optical transition:

$$E_{\text{photon}} = E_{\text{exciton}} \pm E_{\text{magnon}}. \quad (3)$$

The observed upshift in the luminescence can be explained by the case of the upper sign that a photon is created while an exciton and a magnon are annihilated; however, the downshift (corresponding to the lower sign, a photon and a magnon are created and an exciton is annihilated) can be also observed in general. Although it is difficult to conclude the reason why we cannot detect the downshift apparently, the upshift could dominate under the sufficient population of thermally and/or optically excited magnons as reported in a bulk MnF_2 ²⁶.

It would be also fascinating to discuss the magnetic field dependence to unveil detailed features of the interlayer exciton-magnon coupling. In d-d transitions of Mn^{2+} -based bulk materials, it is known that exciton-magnon peaks show almost no Zeeman splitting due to the cancellation coming from the coincidence of optically and magnetically excited states inside Mn^{2+} orbitals^{27,28}. In our case, although there is no comprehensive theory, we can imagine that Zeeman shifts inside Mn^{2+} orbitals can be observed adding to or subtracting from the usual Zeeman splitting in TMDs since no exact cancellation would occur in our interlayer system now. Because the Zeeman splitting in TMDs depends on the valley index (valley Zeeman shift), the g-factor of

such a magnon-coupled valley-exciton would be worth discussing from the theoretical and experimental viewpoints.

Moreover, it would be intriguing to measure such field dependence both in Faraday and Voigt geometries because it would give us the exact easy-axis of the sublattice magnetic moments just at the interface of MnPSe_3 (which can be different from the bulk). This method can be a tool for detecting the surface magnetic ordering of antiferromagnets at heterointerfaces.

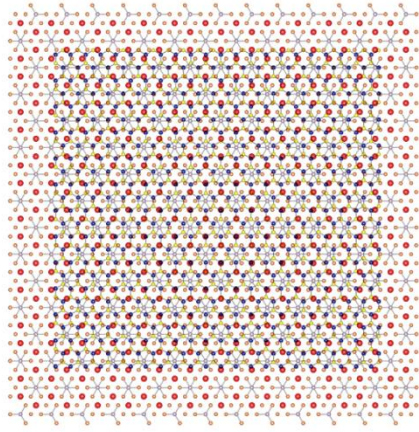
References:

- (1) Flem, G. L., Brec, R., Ouvard, G., Louisy, A. & Segransan, P. Magnetic interactions in the layer compounds MPX_3 ($M = Mn, Fe, Ni$; $X = S, Se$). *J. Phys.: Chem. Solid* **43**, 455-461 (1982).
- (2) Wiedermann, A., Rossat-Mignod, J., Louisy, A., Brec, R. & Rouxel, J. Neutron diffraction study of the layered compounds $MnPSe_3$ and $FePSe_3$. *Solid State Commun.* **40**, 1067-1072 (1981).
- (3) Sivadas, N. *et al.* Gate-Controllable Magneto-optic Kerr Effect in Layered Collinear Antiferromagnets. *Phys. Rev. Lett.* **117**, 267203 (2016).
- (4) Makimura, C., Sekine, T., Tanokura, Y. & Kurosawa, K. Raman scattering in the two-dimensional antiferromagnet $MnPSe_3$. *J. Phys.: Condens. Matter* **5**, 623-632 (1993).
- (5) Kim, K. *et al.* Antiferromagnetic ordering in van der Waals 2D magnetic material $MnPSe_3$ probed by Raman spectroscopy. *2D Mater.* **6**, 041001 (2019).
- (6) Ross, J. S. *et al.* Electrical control of neutral and charged excitons in a monolayer semiconductor. *Nat. Commun.* **4**, 1474 (2013).
- (7) Hao, K. *et al.* Neutral and charged inter-valley biexcitons in monolayer $MoSe_2$. *Nat. Commun.* **8**, 15552 (2017).
- (8) Seyler, K. L. *et al.* Signatures of moiré-trapped valley excitons in $MoSe_2/WSe_2$ heterobilayers. *Nature*. **567**, 66-70 (2019).
- (9) Tran, K. *et al.* Evidence for moiré excitons in van der Waals heterostructures. *Nature*. **567**, 61-75 (2019).
- (10) Jin, C. *et al.* Observation of moiré excitons in WSe_2/WS_2 heterostructure superlattices. *Nature*. **567**, 76-80 (2019).
- (11) Alexeev, E. M. *et al.* Resonantly hybridized excitons in moiré superlattices in van der Waals heterostructures. *Nature*. **567**, 81-86 (2019).
- (12) Wood, C. R. *et al.*, Commensurate–incommensurate transition in graphene on hexagonal boron nitride. *Nat. Phys.* **10**, 451-456 (2014).

- (13) Yoo, H. *et al.*, Atomic and electronic reconstruction at the van der Waals interface in twisted bilayer graphene. *Nat. Mater.* **18**, 448-453 (2019).
- (14) Pak, S. *et al.* Strain-Mediated Interlayer Coupling Effects on the Excitonic Behaviors in an Epitaxially Grown MoS₂/WS₂ van der Waals Heterobilayer. *Nano Lett.* **17**, 5634-5640 (2017).
- (15) Island, J. O. *et al.* Precise and reversible band gap tuning in single-layer MoSe₂ by uniaxial strain. *Nanoscale* **8**, 2589-2593 (2016).
- (16) O'Donnell, K. P. & Chen, X. Temperature dependence of semiconductor band gaps. *Appl. Phys. Lett.* **58**, 2924–2926 (1991).
- (17) Pei, Q., Song, Y., Wang, X., Zou, J. & Mi, W. Superior Electronic Structure in Two-Dimensional MnPSe₃/MoS₂ van der Waals Heterostructures. *Sci. Rep.* **7**, 9504 (2017).
- (18) See <http://www.openmx-square.org/>.
- (19) Scharf, B., Xu, G., Matos-Abiad, A. & Žutić, I. Magnetic Proximity Effects in Transition-Metal Dichalcogenides: Converting Excitons. *Phys. Rev. Lett.* **119**, 127403 (2017).
- (20) Golnik, A., Ginter, J., and Gaj, J. A. Magnetic polarons in exciton luminescence of Cd_{1-x}Mn_xTe. *J. Phys. C: Solid State Phys.*, **16** 6073-6084 (1983).
- (21) Ravets, S. *et al.* Polaron Polaritons in the Integer and Fractional Quantum Hall Regimes. *Phys. Rev. Lett.* **120**, 057401 (2018).
- (22) Tanabe, Y., Moriya, T., Sugano, S. Magnon-Induced Electric Dipole Transition Moment. *Phys. Rev. Lett.* **15**, 1023 (1965).
- (23) Imbusch, G. F., *Luminescence from inorganic solids*, 155-174 (Plenum Press, 1978).
- (24) Zhong, D. *et al.* Van der Waals engineering of ferromagnetic semiconductor heterostructures for spin and valleytronics. *Sci. Adv.* **3**, e1603113 (2017).
- (25) Zhao, C. *et al.* Enhanced valley splitting in monolayer WSe₂ due to magnetic exchange field. *Nat. Nanotechnol.* **12**, 757-762 (2017).

- (26) Tsuboi, T. & Ahmet, P. Temperature dependence of the optical exciton-magnon absorption lines in MnF_2 crystals. *Phys. Rev. B* **45**, 468-470 (1992).
- (27) Sell, D. D. *et al.* Magnetic Effects in the Optical Spectrum of MnF_2 . *J. Appl. Phys.* **37**, 1229-1231 (1966).
- (28) Gnatchenko, S. L., Kachur, I. S. & Piryatinskaya, V. G. Exciton-magnon structure of the optical absorption spectrum of antiferromagnetic MnPS_3 . *Low Temp. Phys.* **37**, 144–148 (2011).
- (29) Cadiz, F. *et al.* Excitonic Linewidth Approaching the Homogeneous Limit in MoS_2 -Based van der Waals Heterostructures. *Phys. Rev. X* **7**, 021026 (2017).

a. Parallel



b. Perpendicular

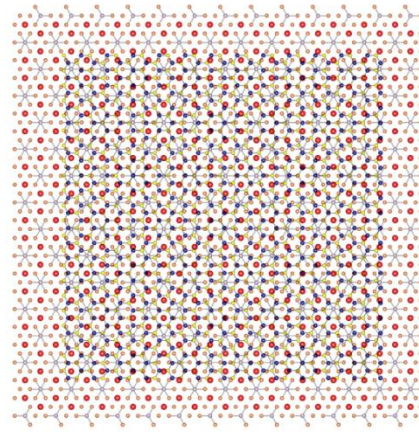


Fig. S1. Stacking images. Top views of MoSe₂/MnPSe₃ with different stacking angles: the zigzag-edge of MoSe₂ parallel to the zigzag-edge of honeycomb Mn²⁺ (same as sample A1, A2, and A3) and the zigzag-edge of MoSe₂ perpendicular to the zigzag-edge of Mn²⁺ (same as sample E1 and E2). Large and small squares are monolayer MnPSe₃ and MoSe₂ films, respectively. The color of each element is same as Fig. 1a except for the selenides in MoSe₂ (yellow here).

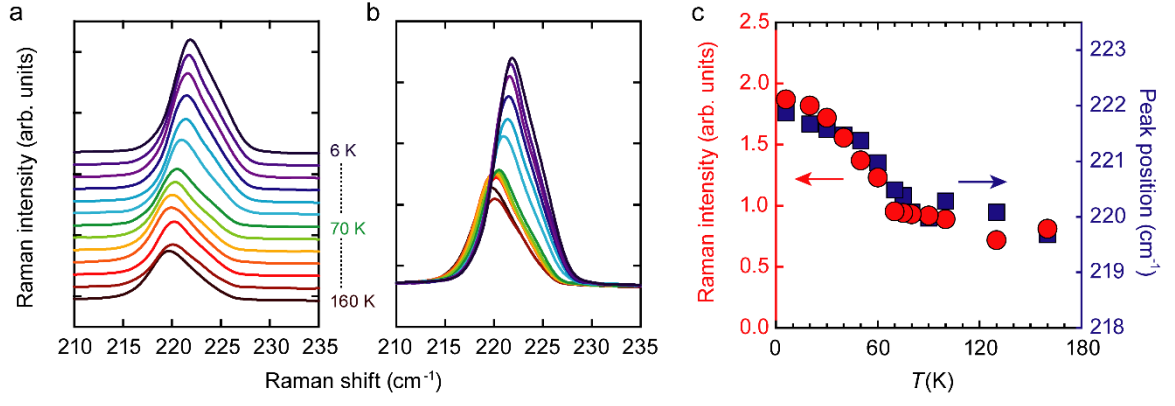


Fig. S2. Raman peak around 222 cm⁻¹ from MnPSe₃. **a, b,** Raman spectra around 220 cm⁻¹ from MnPSe₃ at 6, 20, 30, 40, 50, 60, 70, 75, 80, 90, 100, 130, and 160 K. **c,** Temperature dependence of intensities and positions of the peaks in Fig S2b. Their behaviors change around T_N (= 74 K) of the bulk MnPSe₃.

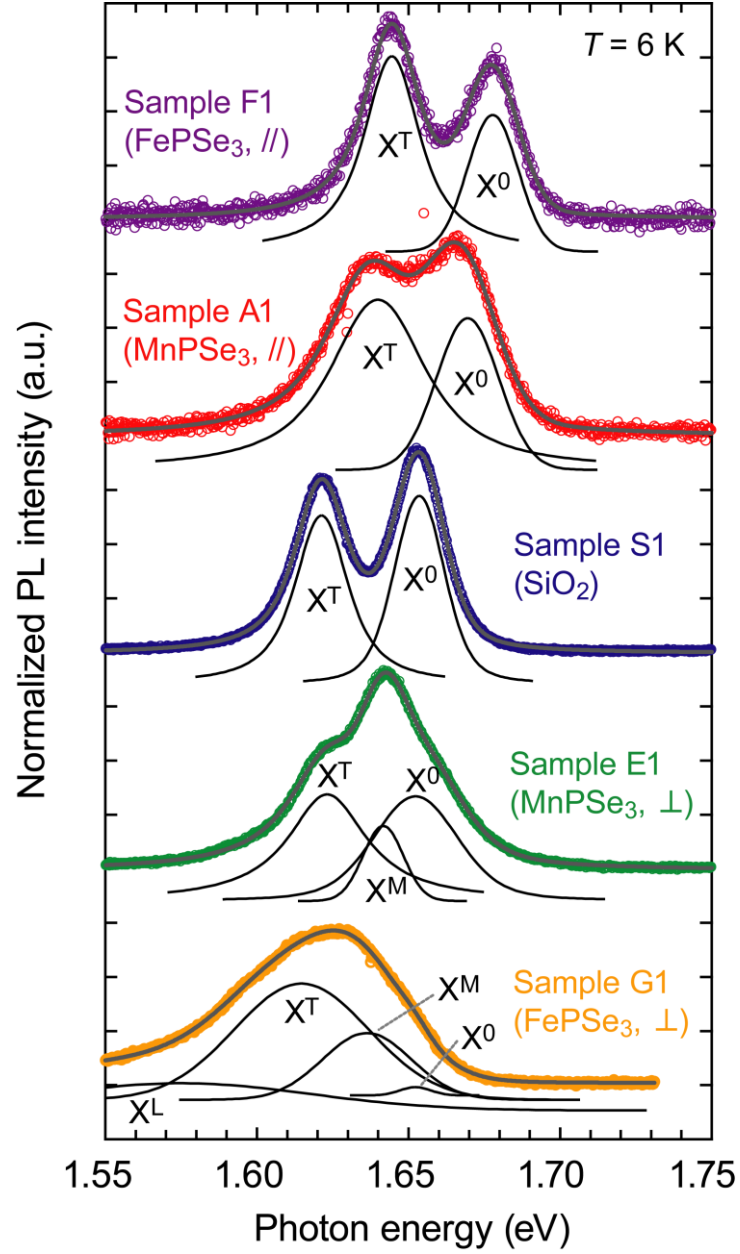


Fig. S3. PL spectra of all MoSe₂/MPSe₃ interfaces. PL spectra from monolayer MoSe₂ in sample F1 (purple), A1 (red), S1 (blue), E1 (green), and G1 (yellow) with the results of the multi-peak fittings by Voigt function. Grey and black lines show the fit traces and peaks for each spectrum, respectively.

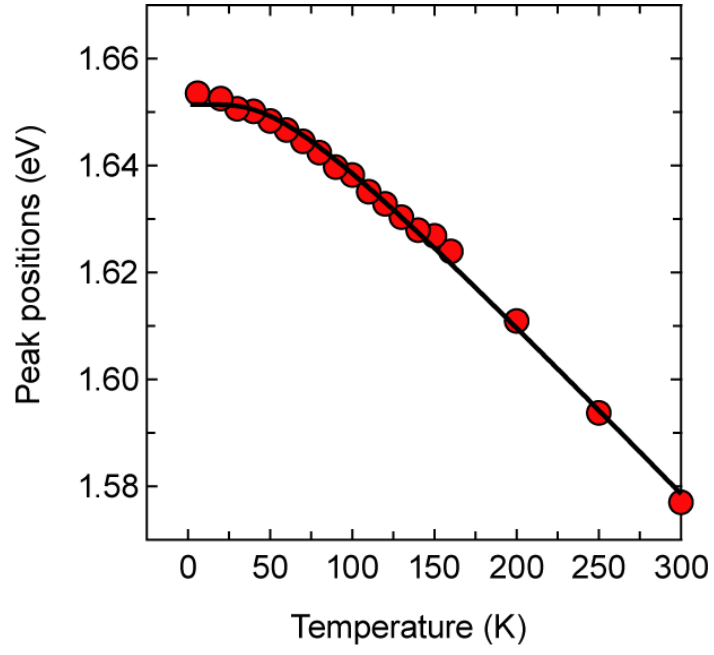


Fig. S4. Temperature dependence of PL peaks in MoSe₂ on SiO₂. The PL peaks of X0 of sample S1 are plotted as a function of temperature with the fitting by (1).

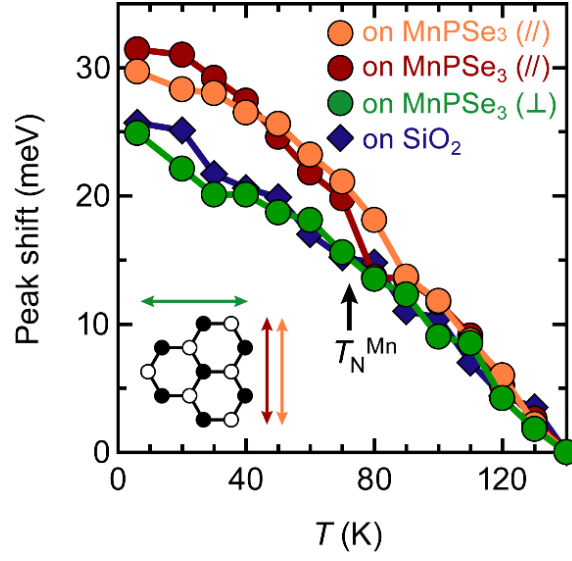


Fig. S5. Temperature dependence in other MoSe₂/MnPSe₃ samples. The PL peak shifts from different MoSe₂ samples from Fig. 4d. Orange and Brown circles correspond to the data from sample A2 and A3 of MoSe₂ on MnPSe₃ with the parallel configuration. Green circles and blue rhombuses come from sample E2 of MoSe₂ on MnPSe₃ with the perpendicular configuration and sample S2 on MoSe₂ on SiO₂, respectively.

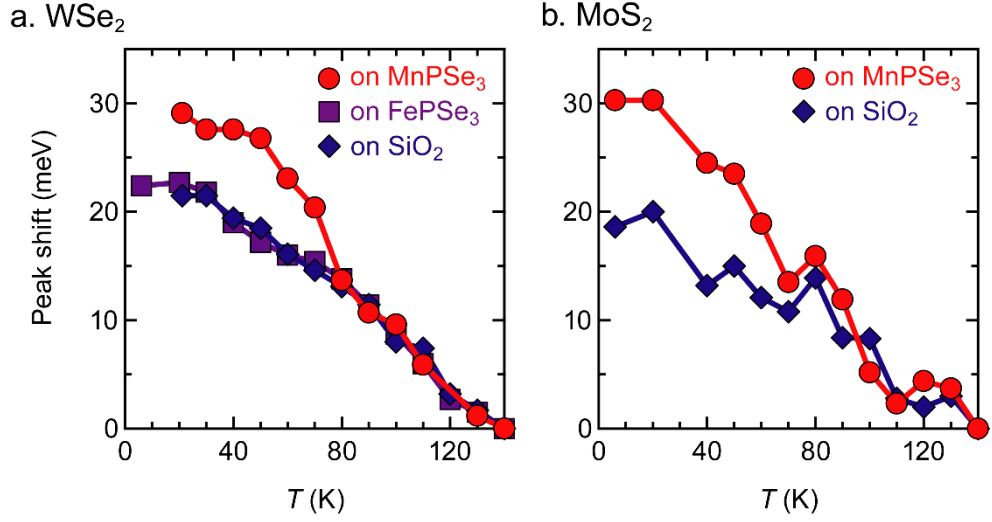


Fig. S6. Peak shifts in the heterointerfaces using WSe₂ and MoS₂. Summary of the shifts of PL peaks from **a** WSe₂ and **b** MoS₂. Red circles, purple squares and blue rhombuses from TMDs on MnPSe₃, FePSe₃ and SiO₂ respectively. Note that the PL peaks from MoS₂ are much broader than others²⁹, which make it difficult to deduce the peak positions precisely by fitting.

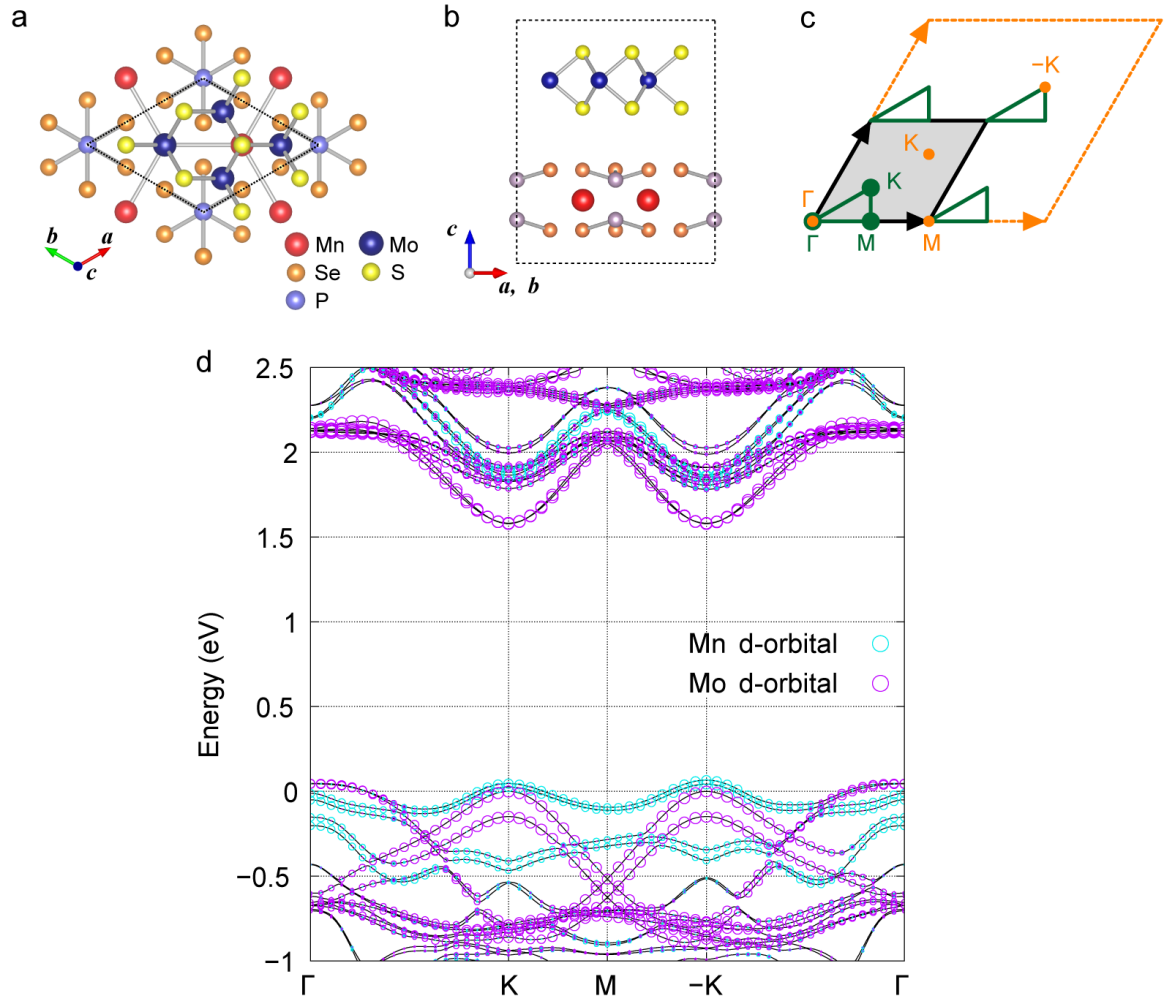


Fig. S7. Electronic band structure of MoS₂/MnPSe₃. **a, b,** Top and side views of the unit cell of the MoS₂/MnPSe₃ bilayer system. **c,** 1st Brillouin zone (BZ) and high-symmetry points for the MoS₂ itself (orange rectangle and letters) and MoS₂/MnPSe₃ superlattice (black rectangle and green letters). The green lines indicate the symmetric lines used for the plots of the band structures in the following. Note that the Γ , K, and M points are the high-symmetry points of the superlattice written in green letters in **c** hereafter. **d,** Electronic band structure of the bilayer system obtained by the GGA+ U calculations ($U = 5$ eV). The radius of cyan and magenta circles indicates the weight of the d orbitals of Mn and Mo, respectively (the Mn-components are multiplied by four for clarity). We set the origin of the energy at the top of the valence band of MoS₂.

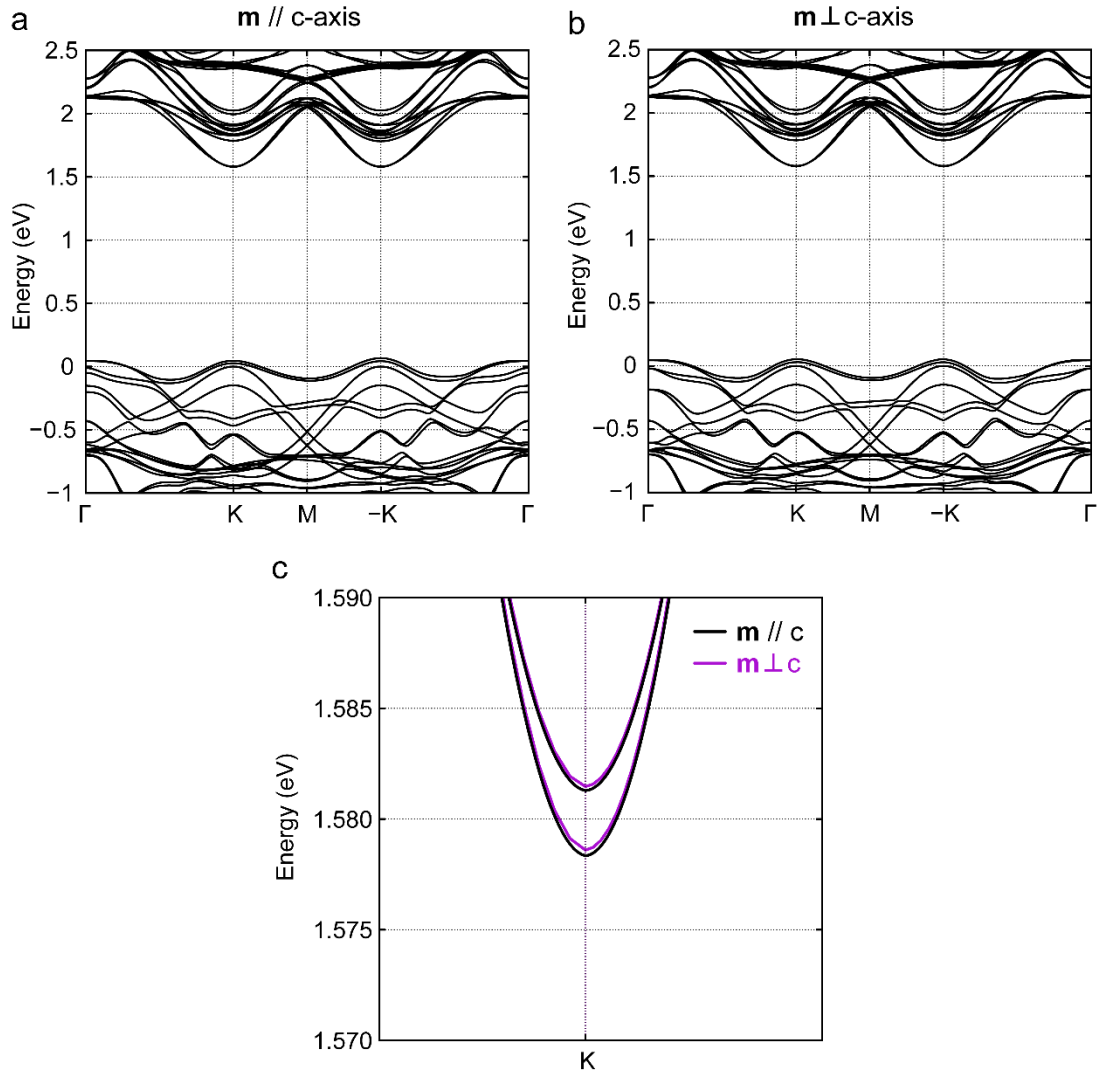


Fig. S8. Magnetization direction dependence of electronic band structures. **a, b,** Electronic band structures obtained by the GGA+ U calculations ($U = 5$ eV) with Néel ordering of **a** $\mathbf{m} // \mathbf{c}$ -axis and **b** $\mathbf{m} \perp \mathbf{c}$ -axis. **c,** Enlarged figure of **a** and **b** around the conduction band bottom of MoS_2 . The difference of the bandgaps (< 0.5 meV) is one order of magnitude smaller than the upshift of the PL spectra observed in experiments (~ 5 meV).

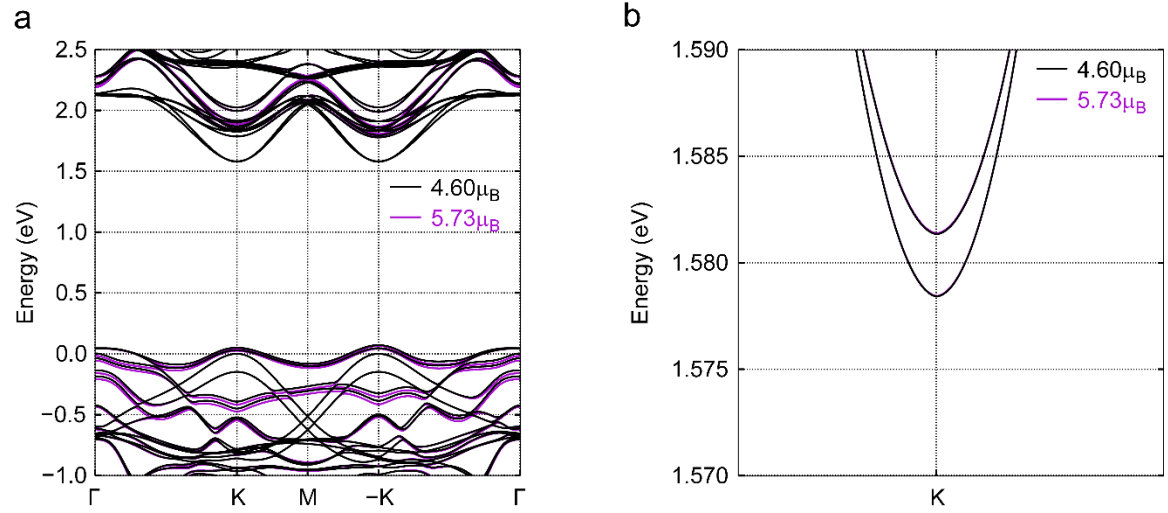


Fig. S9. Magnetic moment dependence of electronic band structures. **a**, Electronic band structures obtained by the GGA+ U calculations ($U = 5$ eV) with the constraints on the magnetic moments of Mn. The black (purple) line shows the results with the magnetic moment $m = 4.60$ (5.73) μ_B along the c axis on each Mn site. **b**, Enlarged figure of **a** around the conduction band bottom of MoS₂. The deduced bandgaps of MoS₂ are almost identical between the two cases.

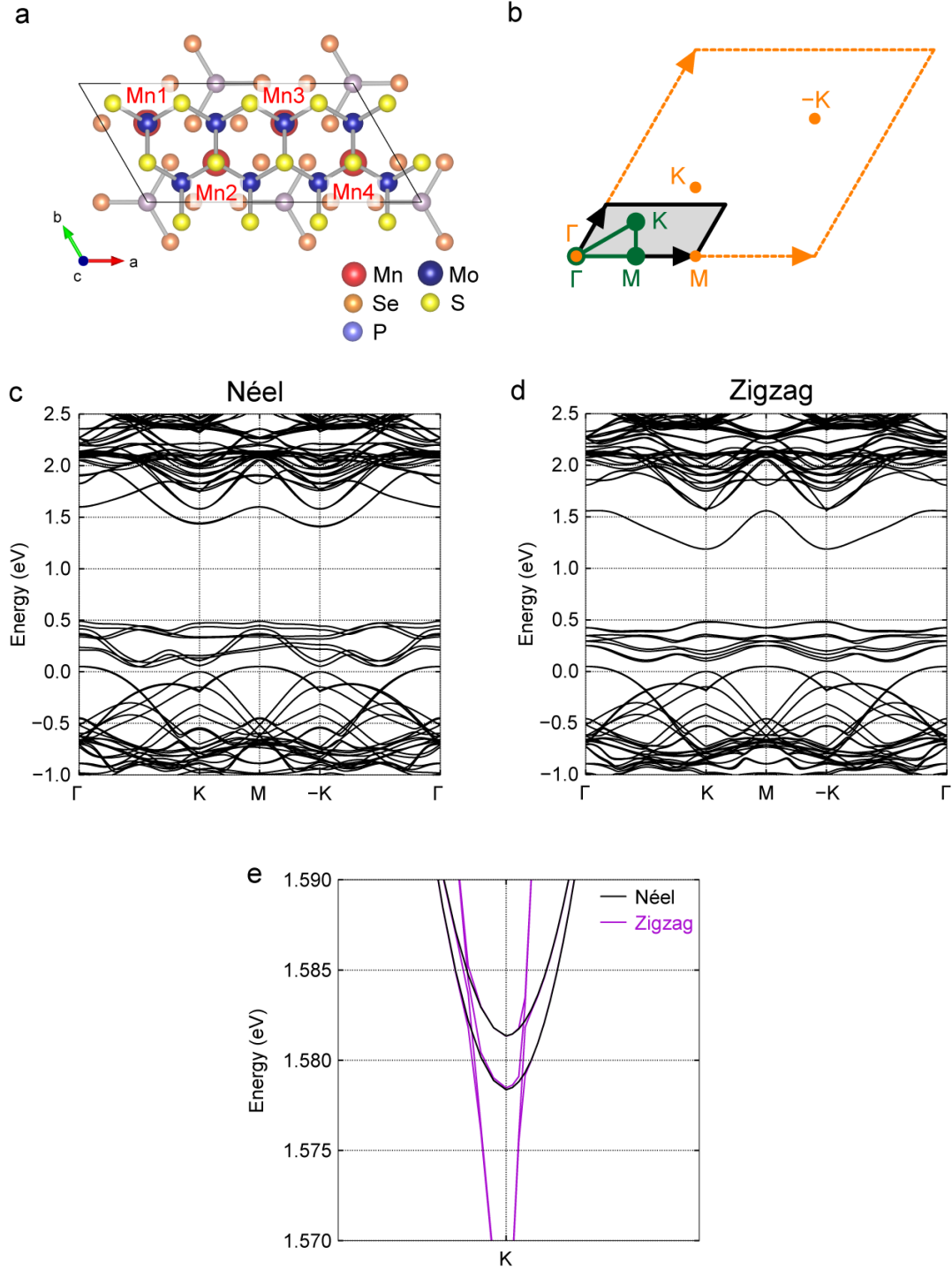


Fig. S10. Antiferromagnetic structure dependence of electronic band structures.

a, The rectangular double supercell including four Mn²⁺ sites (denoted by Mn1, 2, 3, and 4). **b**, 1st Brillouin zone (BZ) for MoS₂ (orange rectangle) and MoS₂/MnPSe₃ double supercell in **a** (black rectangle). Here, we use the same Γ , K, and M points as in Fig. S7c for comparison. Note that the green lines, which are used for the plots of the

band structures in **c** and **d**, are not the symmetry lines for the BZ for this double supercell. **c, d**, Electronic band structures obtained by the GGA calculations with **c** Néel order [Mn1 and 3 (Mn2 and 4) possess up (down) spin along the c axis] and **d** zigzag order [Mn1 and 2 (Mn3 and 4) possess up (down) spin along the c axis]. The kinks at the K points are due to the fact that the Γ -K-M line is not the symmetry line for the doubled supercell. **e**, Enlarged figure around the conduction band bottom of MoS₂. The band structures from MoS₂ are almost identical except for the additional bands from Mn *d* orbitals in the case of zigzag order.

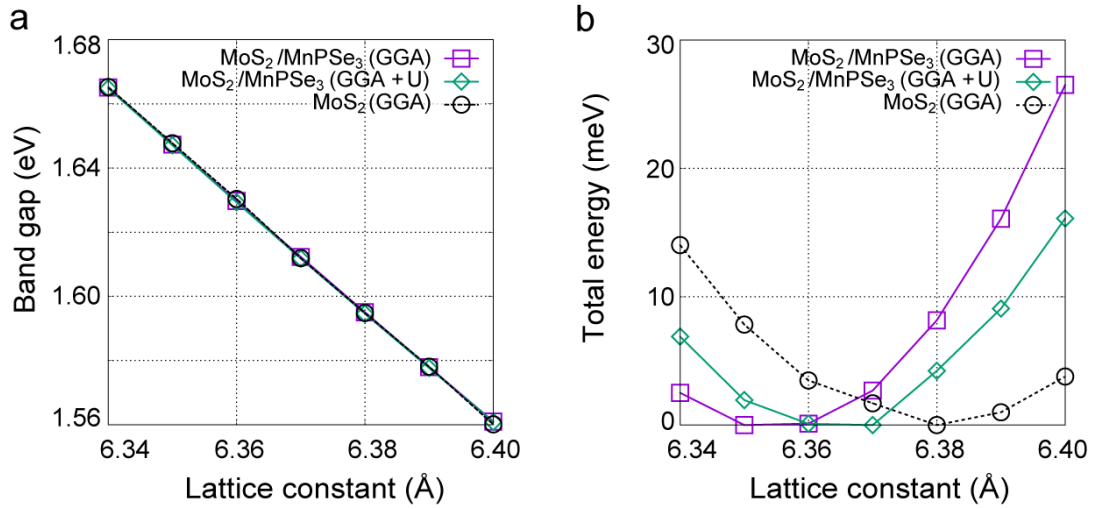


Fig. S11. Lattice constant dependence of bandgap of TMD. **a, b,** Bandgap of MoS₂ and total energy as functions of the lattice constant. The purple, green, and black lines indicate the results by the GGA calculations for the bilayer MoS₂/MnPSe₃, the GGA+ U calculations ($U = 2$ eV) for the bilayer MoS₂/MnPSe₃, and the GGA calculations for the monolayer MoS₂, respectively. In **b**, the total energy is measured from the lowest total energy for each case.